CORA Cork Open Research Archive
Cartlann Taighde Oscailte Chorcaí

Title	Multibeam transmit-reflect-array antenna with switchable bidirectional radiation for IoT applications
Authors	Ma, Yihan;Du, Nijia;Luo, Qi;Ouyang, Xing;Xing, Zijian;Wang, Ling;Yang, Guangwei
Publication date	2026-08-25
Original Citation	Ma, Y, Du, N, Luo, Q, Ouyang, X, Xing, Z, Wang, L & Yang, G 2026, 'Multibeam transmit-reflect-array antenna with switchable bidirectional radiation for IoT applications', IEEE Internet of Things Journal, vol. 13, no. 21, pp. 50468-50480. https://doi.org/10.1109/JIOT.2026.3727129
Type of publication	Article (peer-reviewed)
Link to publisher's version	https://www.scopus.com/pages/publications/105050179031 - 10.1109/JIOT.2026.3727129
Rights	© 2026, IEEE. Personal use of this material is permitted. Permission from IEEE must be obtained for all other uses, in any current or future media, including reprinting/republishing this material for advertising or promotional purposes, creating new collective works, for resale or redistribution to servers or lists, or reuse of any copyrighted component of this work in other works.
Download date	2026-11-06 05:12:21
Item downloaded from	https://hdl.handle.net/10468/19319

UCC
University College Cork, Ireland
Coláiste na hOllscoile Corcaigh

This article has been accepted for publication in IEEE Internet of Things Journal. This is the author's version which has not been fully edited and content may change prior to final publication. Citation information: DOI 10.1109/JIOT.2026.3727129

Multibeam Transmit-Reflect-Array Antenna with Switchable Bidirectional Radiation for IoT applications

Yihan Ma, Nijia Du, Qi Luo, *Member, IEEE*, Xing Ouyang, Zijian Xing, Ling Wang, and Guangwei Yang, *Senior Member, IEEE*

***Abstract*—Exploring cost-effective configurations to achieving wide beam scanning in full-spherical direction is an appealing topic for wireless communications and the Internet of Things (IoT), yet realizing it within the scope of conventional multiple feeding sources reflectarray/transmitarray is extremely challenging. This article proposes a bidirectional multibeam transmit-reflect-array (TRA) using a multi-layer passive metasurface, which enables beam steering switchable between hemispherical and full-spherical directions. First, we demonstrate a novel stacked unit cell composed of a circular ring-based structure and a polarization-sensitive patch structure. Based on the designed unit cell, two 24×24-element arrays are placed above and below the feed antenna, respectively. By simply rotating the angle of the metasurface layers and subsequently exciting the feed antennas, the designed TRA is able to scan beams along the $+z$, $-z$, or $\pm z$ direction. In both unidirectional and bidirectional states, forward and backward beam-scanning is achieved within an angular range of $\pm 55^\circ$, with peak aperture efficiencies of 13.9% and 11.6%, respectively. The measured results of the prototype also demonstrate that the proposed TRA can steer in both unidirectional and bidirectional operating modes. The proposed method opens a new avenue for the design of cost-effective, easy-to-fabricate, and wide-angle beam-scanning multifunctional TRAs, making it particularly suitable for next-generation IoT communication systems that require wide angular coverage and full-space connectivity.**

***Index Terms*—Beamforming, wide-angle coverage, bidirectional radiation, transmit-reflect-array.**

I. Introduction

INTERNET of Things (IoT) networks are typically characterized by dense deployment, random node distribution, and diverse application scenarios, such as industrial automation, unmanned aerial systems, and satellite-assisted mobile communication [1]–[3]. These features impose stringent requirements on wireless systems, including high throughput, seamless coverage, cost-effectiveness, and reliable access.

Driven by the growing demand for high-gain full-space coverage, bidirectional transmit-reflect-array (TRA) antennas have attracted increasing research interest. One representative application is UAV-based space–air–ground emergency communication, where low-profile and lightweight conformal TRAs can be integrated with aerial platforms. In [4], a dual-band shared-aperture conformal TRA provides independently controlled 35-GHz reflective air-to-ground and 140-GHz transmissive air-to-satellite links on a single UAV platform. At the network level, a UAV can also work as a temporary relay when terrestrial communication infrastructure is damaged. In [5], the UAV collects data and harvests energy from one disconnected IoT network through simultaneous wireless information and power transfer (SWIPT), and then moves to another network to forward the collected data to its base station.

On the other hand, passive wide-coverage TRAs can also be used in low-cost fixed IoT systems. Two representative applications are vehicle-to-infrastructure (V2I) and outdoor-to-indoor (O2I) communications. In V2I systems, roadside units require forward, backward, or bidirectional coverage to communicate with approaching and departing vehicles under slowly varying traffic conditions [6]. In O2I systems, millimeter-wave signals suffer from high penetration loss through walls and windows. Transmitarray installed on building facades or windows can improve the communication coverage between outdoor infrastructure and indoor users [7], [8]. These fixed applications are less sensitive to antenna profile, and their coverage modes normally change slowly. Since many roadside or building-mounted units may be required, passive bidirectional apertures are attractive because of their low fabrication cost and low control-power consumption.

To meet these demands, directional and multibeam beamforming techniques are widely adopted to concentrate electromagnetic energy in desired directions, thereby enhancing signal quality and improving spectral efficiency [9]–[12]. For example, a notable design based on a unit cell incorporating a cylindrical dielectric resonator was presented in [11] for the development of a high-gain dielectric reflectarray. By varying the radius of the unit cell, a full 360° reflection phase coverage can be achieved, resulting in a measured peak antenna gain of 23.9 dBi. More recently, to realize wide-angle beam scanning with stable gain, an FPGA-based pattern-reconfigurable metasurface has been proposed, achieving beam steering over a range from 0° to 60° with a gain variation of less than 2 dB [12]. In addition, irregular subarray configuration is also attracting researchers' attention in recent years due to its ability in balance fabrication cost and radiation efficiency [14]–[16]. In contrast to conventional phased arrays, domino-shaped subarray configurations generally exhibit a slight deterioration in realized gain and sidelobe levels (SLLs) [15].

Manuscript submitted on 16 September 2025. This work was supported by the Fundamental Research Funds for the Central Universities under Grant G2025KY05082, and in part by the Natural Science Basic Research Program of Shaanxi Program under Grant 2025JC-YBMS-739 and Newton International Fellowships Alumni AL\24100018. *(Corresponding author: Guangwei Yang.)*

Yihan Ma, Nijia Du, Zijian Xing, Ling Wang, and Guangwei Yang are with School of Electronics and Information, Northwestern Polytechnical University, Xi'an Shaanxi,710129, P.R.China.(E-mail: nwpu.mayihan@gmail.com; guangwei.yang@nwpu.edu.cn).

Qi Luo is with the School of Physics, Engineering and Computer Science, University of Hertfordshire, Hertfordshire, AL10 9AB, UK (email: q.luo2@herts.ac.uk).

Xing Ouyang is with the Photonic Center, Tyndall National Institute, University College Cork, Cork, T12 R5CP, Ireland (email: xing.ouyang@tyndall.ie).

Authorized licensed use limited to: UNIVERSITY COLLEGE CORK. Downloaded on September 23,2026 at 13:28:03 UTC from IEEE Xplore. Restrictions apply.
© 2026 IEEE. All rights reserved, including rights for text and data mining and training of artificial intelligence and similar technologies. Personal use is permitted, but republication/redistribution requires IEEE permission. See https://www.ieee.org/publications/rights/index.html for more information.

This article has been accepted for publication in IEEE Internet of Things Journal. This is the author's version which has not been fully edited and content may change prior to final publication. Citation information: DOI 10.1109/JIOT.2026.3727129

More recently, the incorporation of deep learning (DL)-based techniques into phased arrays has also been investigated, with the aim of accelerating subarray configuration optimization and achieving accurate beamforming performance with high efficiency in large-scale irregular subarray apertures [16].

Nevertheless, traditional transmitarrays and reflectarrays typically radiate in only one direction, which significantly limits communication coverage. In recent years, many emerging IoT applications operate in three-dimensional (3D) environments, where communications may occur between ground users, aerial platforms, and infrastructure nodes, leading to stringent requirements on full-spherical coverage capability [17]. Fig. 1 illustrates the beam-steerable metasurface antenna configurations applied in both unidirectional and bidirectional scenarios. To address these challenges, bidirectional beam-scanning configurations have attracted increasing research attention. One common approach to achieving bidirectional beam scanning involves the use of pattern-reconfigurable antenna elements [22], [23]. For instance, by appropriately selecting short pins beneath a circular patch, a patch antenna exhibiting quasi-bidirectional patterns at 3.4 GHz with a peak gain of 7.3 dBi was proposed in [22]. Although such pattern-reconfigurable arrays are capable of bidirectional beam scanning, simultaneous beam steering for both transmitter and receiver channels remains a challenge. While the addition of transmit/receive (T/R) modules to each element can enable independent bidirectional beam scanning, this approach results in high fabrication costs [24].

To address the need for full-scope coverage with high gain and low fabrication cost, transmit-reflect-array antennas (TRAs), which integrate reflectarray and transmitarray functionalities, have been widely explored in recent years. These devices can generally be classified as frequency-selective TRAs and polarization-dependent TRAs. Frequency-selective TRAs enable the transmitarray and reflectarray to operate at different frequencies [25]–[27]. For example, in [25] the authors employed a frequency-selective surface (FSS) as the ground plane for a reflectarray operating at 9 GHz and as a transparent surface for a transmitarray operating at 12 GHz, thereby achieving simultaneous reflection and transmission at distinct frequencies. In contrast, polarization-dependent TRAs handle differently polarized waves in the forward and backward directions [28]–[30], [32]. A novel TRA proposed in [29] utilized two orthogonal polarization grids printed on substrates to achieve bidirectional beam scanning for different incident polarizations; for the *x*-polarized incident wave, the grids function as a reflector, whereas for the *y*-polarized wave, they serve as a polarization converter to enable transmission through the unit cell.

More recently, electrically addressable TRAs have garnered extensive attention due to their rapid response and precise beamforming control [33]–[36]. In 2019, an innovative single-layer, 1-bit electronically reconfigurable bidirectional TRA based on a slot element was proposed to simultaneously transmit and reflect waves [33]. Subsequently, a patch-shaped reconfigurable unit cell integrating two PIN diodes was introduced to achieve polarization switching via controlled ON/OFF states, enabling the TRA to alternate between simultaneous and time-division operating modes [34]. However, the large number of PIN diodes and the complex control circuitry significantly increase the overall complexity and fabrication cost, limiting their suitability for cost-sensitive applications.

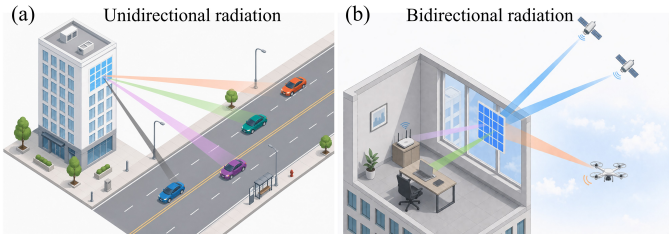


Fig. 1. Conceptual use cases of unidirectional and bidirectional beam-steerable metasurface antennas for IoT communications: (a) unidirectional scenario; (b) bidirectional scenario.

To balance design complexity with beam scanning performance, multibeam scan reflectarray methodologies have been investigated [37]–[41]. Rather than employing reconfigurable unit cells for beam manipulation, a multi-feed configuration can steer beams in different directions via a passive metasurface. In [37], Yu et al. proposed a novel circularly polarized folded reflectarray antenna configuration with 15 feeding ports that achieved beam steering from -29° to $+29^\circ$, with a maximum gain of 24.6 dBic. In this configuration, each feed scans a beam in a single direction without phase modulation on the antenna elements. Furthermore, an iterative optimization algorithm was employed to modulate beam intensity at different directions [40]. However, conventional reflectarrays can typically achieve beam scanning only within a hemispherical range, which is insufficient for applications requiring bidirectional communication. More recently, Qin et al. proposed a novel multi-port feeding TRA that combines a transmitarray with a folded transmitarray to realize switchable multibeam scanning in both forward and backward directions [41]. In the hemispherical scanning state, a maximum scanning range of –30° to +30° was achieved with peak gains of 23.6 dBi, whereas in the bidirectional scanning state the maximum scanning angles were 40° for the forward direction and 22° for the backward direction. Despite these advancements, the scanning ranges of state-of-the-art hybrid TRAs and many multibeam reflectarrays and transmitarrays remain limited to approximately 30° due to inherent design constraints.

Motivated by these observations, the primary objective of this article is to propose a multibeam TRA configuration capable of wide-angle beam scanning in both unidirectional and bidirectional modes, either separately or simultaneously. The proposed TRA consists of two polarization-sensitive stacked metasurfaces and seven patch dipole antennas, with the radiation direction being switchable through simple rotation of the unit cells. To the best of the authors' knowledge, this work represents the first demonstration of a stacked unit cell configuration that achieves wide-angle beam scanning in both hemispherical and full-sphere radiation modes via rotation control of the polarization grids and unit cell.

This paper is organized as follows. Section II presents the structure of the proposed unit cell. Section III describes the

Authorized licensed use limited to: UNIVERSITY COLLEGE CORK. Downloaded on September 23,2026 at 13:28:03 UTC from IEEE Xplore. Restrictions apply.
© 2026 IEEE. All rights reserved, including rights for text and data mining and training of artificial intelligence and similar technologies. Personal use is permitted, but republication/redistribution requires IEEE permission. See https://www.ieee.org/publications/rights/index.html for more information.

This article has been accepted for publication in IEEE Internet of Things Journal. This is the author's version which has not been fully edited and content may change prior to final publication. Citation information: DOI 10.1109/JIOT.2026.3727129

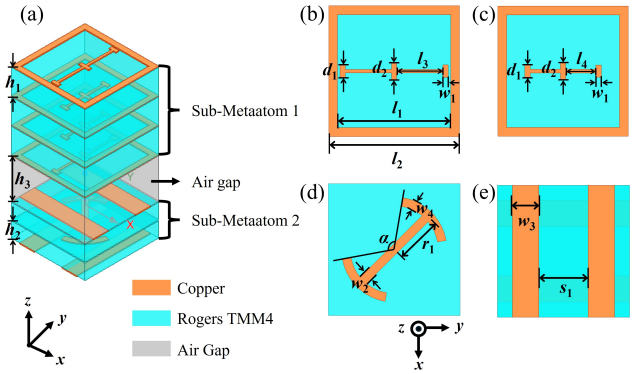


Fig. 2. (a) Perspective of the stacked metaatom structure. Details of (b) top layer of sub-metaatom 1, (c) middle layer of sub-metaatom 1, (d) top layer of sub-metaatom 2, (e) middle layer of sub-metaatom 2. The geometry parameters are listed as: $h_1 = 2.5\ mm$, $h_2 = 1.524\ mm$, $h_3 = 4.0\ mm$, $d_1 = 0.7\ mm$, $d_2 = 1.0\ mm$, $w_1 = 0.3\ mm$, $w_2 = 0.5\ mm$, $w_3 = 1.5\ mm$, $w_4 = 0.5\ mm$, $l_1 = 6.5\ mm$, $l_2 = 7.5\ mm$, $s_1 = 2.8\ mm$, $r_1 = 2.5\ mm$.

operating principle of the multibeam TRA and provides a theoretical analysis of the TRA beamforming mechanism. Section IV details the implementation and experimental validation of the designed TRA operating in both unidirectional and bidirectional modes. Finally, Section V concludes the paper.

II. Unit Cell Design

To realize the proposed wide-angle beam steering TRA configuration, a stacked metasurface configuration with two polarization-sensitive sub-metaatom structures is designed in this work. The overall configuration of stacked unit cell is shown in Fig. 2a. An air gap of height h_3 is sandwiched between sub-metaatom 1 and sub-metaatom 2.

A. Sub-metaatom 1

The sub-metaatom 1 is a four-layer cascaded ABBA structure incorporating patches and a square mesh. The patches in layers 1 and 4 are identical, as are those in layers 2 and 3, and the square mesh is consistent across all four layers. By controlling the mutual interaction via the lengths of the patches and their corresponding branches, high transmission efficiency can be achieved over a 320° phase variation range, enabling polarization-dependent directional control [42]. Fig. 2b and 2c show the parameter details of layer 1 and layer 2. Three identical substrates Rogers TMM4 with a dielectric constant $\varepsilon_r = 4.5$, $\tan\delta = 0.002$, and a thickness of h_1 are employed to cascade ABBA structure. Varying the length of patches along the y-axis introduces different transmission phases, and tuning the length of the branches provides additional flexibility to suppress fluctuations in the transmission amplitude. Under normal incidence illuminated along the y-axis, a 320° phase coverage with highly efficient transmission amplitude is achieved. In contrast, for an x-polarized incident wave, a nearly constant transmission phase is realized, indicating that the sub-structure exhibits polarization-sensitive behaviour. A detailed description of transmission amplitude and phase of sub-metaatom 1 by changing the parameters l_3 from 2.6 mm to 6.2 mm and Δl, defined as $l_3 - l_4$ from 0.3 mm to 1.0 mm at 10 GHz is depicted in Fig. 3.

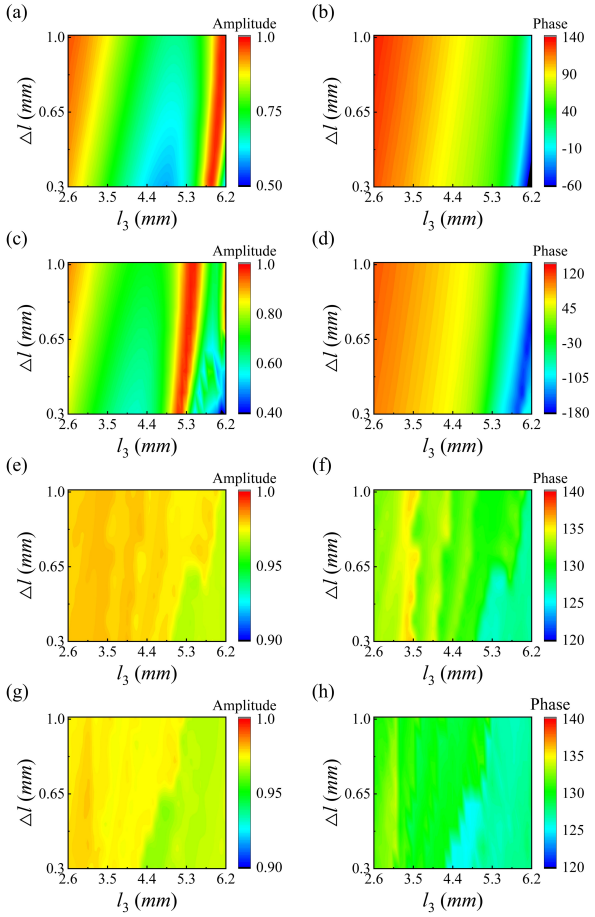


Fig. 3. Transmission amplitude for (a) $d_1 = 0mm$ with a y-polarized incident wave, (c) $d_1 = 0.5mm$ with a y-polarized incident wave, (e) $d_1 = 0mm$ with a x-polarized incident wave, (g) $d_1 = 0.5mm$ with a x-polarized incident wave, at the frequency of 10 GHz. Transmission phase response for (b) $d_1 = 0mm$ with a y-polarized incident wave, (d) $d_1 = 0.5mm$ with a y-polarized incident wave, (f) $d_1 = 0mm$ with a x-polarized incident wave, (h) $d_1 = 0.5mm$ with a x-polarized incident wave, at the frequency of 10 GHz.

As can be observed from Fig. 3a and 3b, under y-polarized incident wave, most of the transmission amplitude is maintained over 0.75, and the transmission phase ranges from $-57°$ to $140°$ when $d_1 = 0$ mm. To guarantee a larger transmitted phase coverage for sub-metaatom 1 structure, the transmission coefficient of the metaatom when $d_1 = 0.5$ mm is also investigated. As shown in Fig. 3c and 3d, under y-polarized incident wave, the transmission phase of the metaatom ranges from $-180°$ to $120°$. By combining the metaatom with $d_1 = 0$ mm and $d_1 = 0.5$ mm, sub-metaatom 1 is able to cover the transmission phase ranging from $-180°$ to $160°$. Fig. 3e to 3h present the variation of transmission amplitude and phase of metaatom under x-polarized incident wave. It can be clearly observed that slight fluctuations appear in the transmission amplitude, which remains higher than 0.92 in all cases, while the transmission phase remains nearly constant across all scenarios. Therefore, sub-metaatom 1 is a polarization-sensitive structure that resonates with one predefined polarization and becomes transparent to the cross-polarized wave.

Authorized licensed use limited to: UNIVERSITY COLLEGE CORK. Downloaded on September 23,2026 at 13:28:03 UTC from IEEE Xplore. Restrictions apply.
© 2026 IEEE. All rights reserved, including rights for text and data mining and training of artificial intelligence and similar technologies. Personal use is permitted, but republication/redistribution requires IEEE permission. See https://www.ieee.org/publications/rights/index.html for more information.

This article has been accepted for publication in IEEE Internet of Things Journal. This is the author's version which has not been fully edited and content may change prior to final publication. Citation information: DOI 10.1109/JIOT.2026.3727129

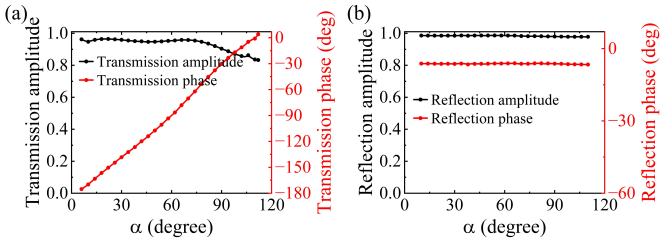


Fig. 4. Simulated (a) transmission amplitude and phase and (b) reflection amplitude and phase response with different parameter α for sub-metaatom 2 at the frequency of 10 GHz.

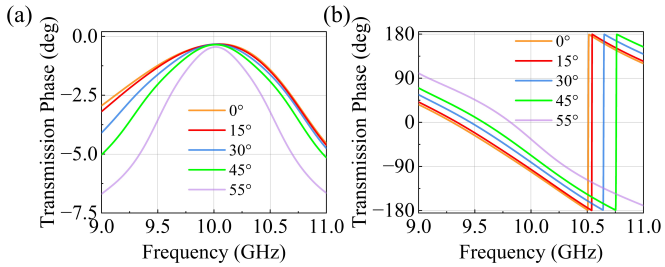


Fig. 5. Simulated transmission spectra for the stacked meta-atom under oblique incidence. (a) Transmission amplitude and (b) transmission phase.

B. Sub-metaatom 2

The sub-metaatom 2 consists of two identical Rogers TMM4 substrates, each with a thickness of h_2. Two parallel metal gratings with two orthogonal pairs are placed on the top layer and bottom layer of sub-metaatom 2, and the middle layer contains a circular ring with a diagonal metal bar structure [43]. The metal gratings are capable of imparting a 90° polarization rotation to the y-polarized transmitted wave along the $+z$-axis direction, while blocking the x-polarized transmitted wave along the same direction due to the strong inductance effect caused by the metal gratings. When the circular ring structure encounters the y-polarized transmitted wave, its two arc rings generate surface currents in opposite directions along the y-axis and in the same direction along the x-axis. The overall result is that the x-polarized incident waves are converted to their orthogonal polarization. A 180° phase coverage can be obtained by tuning the geometric parameters, specifically when α is adjusted within the range of 5° to 115°. By simply flipping the circular ring structure along the x-axis, an additional 180° phase shift can be achieved for the y-polarized direction. It can be clearly observed from Fig. 4a that the metaatom can induce a phase change between -180° and 0° when the parameter α changes from 5° to 115°. At the same time, the transmission efficiency remains above 0.82 in all cases. When illuminated by x-polarized incident waves, the metal grating fully reflects the incident wave, serving as a conductive ground plane. The reflection phase is nearly constant, and the reflection amplitude remains above 0.95 in all cases, as can be clearly observed in Fig. 4b.

In summary, linear polarization conversion is provided by the sub-metaatom-2 layer. The metasurface transmission coefficient is controlled jointly by the sub-metaatom-1 and sub-metaatom-2 layers. When the rotated patches of sub-metaatom 1 are oriented parallel to the x-axis, only sub-metaatom 2 influences the transmission phase. Conversely, when the rotated patches of sub-metaatom 1 are perpendicular to the x-axis, the transmission phase is determined by both layers.

Following the normal-incidence analysis, the oblique-incidence response of the proposed metaatom is evaluated in Fig. 5. At 10 GHz, the transmission magnitude remains between -0.335 and -0.455 dB for incidence angles from 0° to 55°, showing good magnitude stability. Compared with normal incidence, the phase deviations are approximately 4.6°, 19.2°, 33.3°, and 66.3° at 15°, 30°, 45°, and 55°, respectively. Therefore, the phase variation remains moderate up to 45°, but becomes more evident at 55°.

Note that, due to coupling effects between sub-metaatom 1 and sub-metaatom 2, variations in the parameter α can adversely affect the transmission coefficient. Therefore, the geometric parameters of sub-metaatom 1 need to be fine-tuned to achieve an accurate transmission coefficient when integrating sub-metaatom 2 into the complete unit cell.

III. Operating Principle

To realize a transmissive-reflective array (TRA) capable of wide-angle scanning while switching between backward reflection and forward transmission modes, a polarization-sensitive rotatable unit cell is investigated. This design facilitates beam scanning up to a maximum angle of 60°. Fig. 6 depicts the working principle of the proposed TRA for beam scanning in both unidirectional and bidirectional radiation scenarios. By independently varying the rotation states of the sub-metaatom 1 and sub-metaatom 2 metasurfaces, four distinct combinations are achieved, enabling the incident wave to be radiated in different directions and at different angles. Fig. 6a to 6c illustrate three different rotation states of the stacked metasurface. In transmit mode 1 (TM1), the bottom metal grating in sub-metaatom 2 is oriented parallel to the y-axis, and the patches in sub-metaatom 1 are aligned perpendicular to the x-axis. In reflect mode 1 (RM1), the bottom metal grating in sub-metaatom 2 is perpendicular to the y-axis. In transmit mode 2 (TM2), the bottom metal grating in sub-metaatom 2 is again parallel to the y-axis, while the patches in sub-metaatom 1 are parallel to the x-axis. Based on these mode combinations, switchable bidirectional beams are realized as follows:

Bidirectional small steering angles: Seven printed dipole antennas A1 to A7, serving as feeds, are symmetrically positioned along the x-axis between the upper and lower metasurfaces, with both metasurfaces in the rotation state TM1. When illuminated by x-polarized incident waves from the feed antennas, the upper and lower metasurfaces can radiate a y-polarized pencil beam in the forward and backward directions separately, as shown in Fig. 6d. In TM1, the steering angles of the TRA are manipulated by the transmission phase of sub-metaatom 2, where the sub-metaatom 1 has little to no impact on the steering beams.

Bidirectional large steering angles: To realize larger steering angles, sub-metaatom 1 is rotated to introduce additional

Authorized licensed use limited to: UNIVERSITY COLLEGE CORK. Downloaded on September 23,2026 at 13:28:03 UTC from IEEE Xplore. Restrictions apply.
© 2026 IEEE. All rights reserved, including rights for text and data mining and training of artificial intelligence and similar technologies. Personal use is permitted, but republication/redistribution requires IEEE permission. See https://www.ieee.org/publications/rights/index.html for more information.

This article has been accepted for publication in IEEE Internet of Things Journal. This is the author's version which has not been fully edited and content may change prior to final publication. Citation information: DOI 10.1109/JIOT.2026.3727129

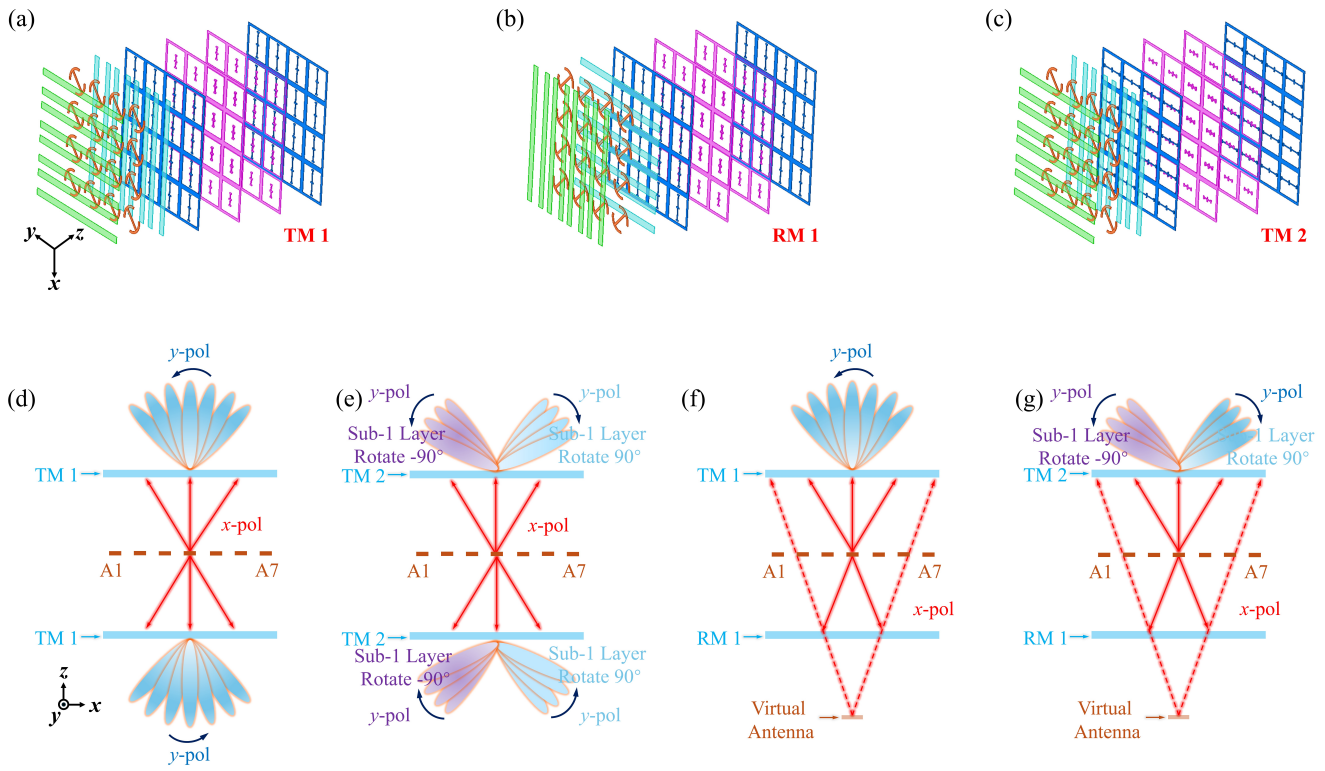


Fig. 6. Rotation states of metasurface in (a) TM1, (b) RM1, (c) TM2. Schematics of the proposed beam switchable antenna in (d) bidirectional small angle steering, (e) bidirectional large angle steering, (f) unidirectional small angle steering, (g) unidirectional large angle steering.

transmission phase (see Fig. 6(e)). A clockwise 90° rotation produces a pencil beam at positive elevation, whereas an anticlockwise 90° rotation produces a pencil beam at negative elevation, because the phase distribution is mirrored about the yoz-plane when sub-metaatom 1 is switched between the two states. The pencil beams are symmetric about the yoz-plane when the feed ports are sequentially excited from A1 to A4 or from A7 to A4. Owing to the metal grating in sub-metaatom 2, an x-polarized excitation yields y-polarized pencil beams in both the forward and backward directions.

Unidirectional small steering angles: When sub-metaatom 2 on one side of the TRA is rotated by 90°, the metal grating behaves as a conducting ground plane that fully reflects the incident wave without altering its polarization. By image theory, the antenna can be modeled by a virtual source at the mirror position. In this case, the phase distribution of the upper metasurface is determined by the real feed antennas and their corresponding virtual images. The corresponding rotation state radiating toward the $+z$-axis is shown in Fig. 6(f).

Unidirectional large steering angles: By switching the upper metasurface from TM1 to TM2, the proposed TRA radiates beams with large scan angles toward the $+z$-axis. In this configuration, the RM1 metasurface acts as a conducting ground plane that fully reflects the incident wave. Consequently, the upper metasurface is influenced by both the real feed ports and their virtual ports, which jointly determine the radiation performance. As in the large-angle bidirectional mode, rotating sub-metaatom 1 clockwise or anticlockwise by 90° produces positive or negative elevation scans, respectively.

IV. Transmit-Reflect-Antenna Design

A. Design of Feeding Antenna

A classical printed dipole antenna is employed to ensure bidirectional beam radiation on the metasurfaces. In this TRA, a linear array consisting of seven identical printed dipole antennas, each individually fed by a coaxial cable, is located at the midpoint between the two metasurfaces. The dipoles are printed on both sides of a Rogers RO4003C substrate material ($\varepsilon_r = 3.55$ and $\tan\delta = 0.0027$) with a thickness of $h_4 = 0.26$ mm, and a 50-ohm coaxial cable is used to feed and support the dipoles. The central distance between two adjacent dipoles is $d = 0.35\lambda$. The configuration of printed dipole and its corresponding S-parameters are shown in Fig. 7a and 7b, separately. The radiation pattern in Fig. 7c exhibits a bidirectional beam with a maximum realized gain of 2.1 dBi in the E-plane.

B. Design of Metasurface Phase Distribution

In single-focus phase designs, the required phase of the mnth unit cell for the ith radiation beam direction is defined as:

$$\varphi_{mn}^{(i)} = k_0 \left[|\vec{r}_{mn} - \vec{r}_f| - \sin\theta^{(i)} \left(x_{mn}\cos\varphi^{(i)} + y_{mn}\sin\varphi^{(i)} \right) \right] \tag{1}$$

where k_0 represents the wavenumber in the vacuum, $\theta^{(i)}$ and $\phi^{(i)}$ are the elevation and azimuth angle of ith designed beam, respectively. $\vec{r}_{mn} = (x_{mn}, y_{mn}, z_{mn})$ is the position

Authorized licensed use limited to: UNIVERSITY COLLEGE CORK. Downloaded on September 23,2026 at 13:28:03 UTC from IEEE Xplore. Restrictions apply.
© 2026 IEEE. All rights reserved, including rights for text and data mining and training of artificial intelligence and similar technologies. Personal use is permitted, but republication/redistribution requires IEEE permission. See https://www.ieee.org/publications/rights/index.html for more information.

This article has been accepted for publication in IEEE Internet of Things Journal. This is the author's version which has not been fully edited and content may change prior to final publication. Citation information: DOI 10.1109/JIOT.2026.3727129

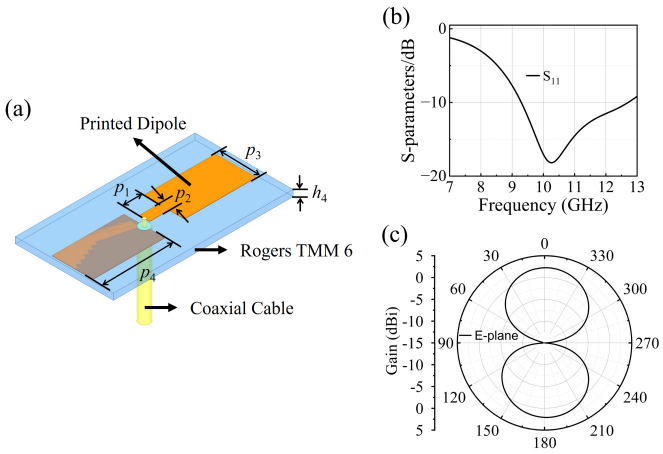


Fig. 7. (a) 3D view of feed antenna. The optimized dimensions are p_1=1.2 mm, p_2=0.65 mm, p_3=2.5 mm, p_4=4.4 mm. (b) Simulated S_{11} parameters of feed antenna. (c) Radiation patterns of feed antenna.

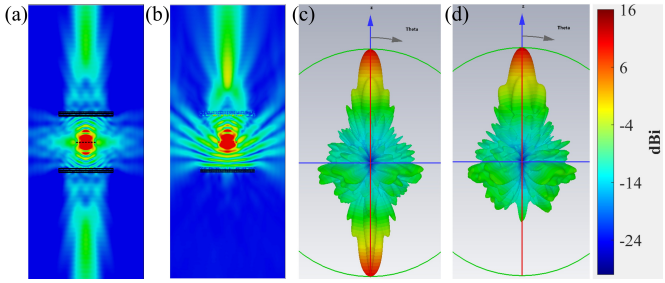


Fig. 8. (a) Simulated E-field distribution and (c) its corresponding 3D radiation pattern in transmit mode. (b) Simulated E-field distribution and (d) its corresponding 3D radiation pattern in reflect mode.

vector of the mnth element, $\vec{r}_f = (x_q, 0, 0)$ is the position vector of feed phase center. In a passive metasurface design, a metaatom exhibits a single transmission coefficient. To guarantee a multibeam scanning, a multifocal phase correction of metasurface based on averaged phase distribution can be obtained as follows:

$$\varphi_{mn}^{ave} = (\sum_{i=1}^{Q} \varphi_{mn}^{(i)})/Q \tag{2}$$

where Q is the number of designed beams. In this design, when TRA operates in bidirectional and unidirectional small steering angles states, the value of φ_{mn}^{ave} is entirely decided by the sub-metaatom 2 layers. For bidirectional and unidirectional large-angle modes, the φ_{mn}^{ave} is determined by both sub-metaatom 1 layers and sub-metaatom 2 layers togethers.

Specifically, in the bidirectional radiation mode, the transmission response of the mnth meta-atom in the sub-metaatom 2 layers illuminated by the qth feed can be described using the Jones matrix as:

$$\mathbf{T}_{mn}^{(q)} = \begin{bmatrix} t_{xx,mn}^{(q)} & t_{xy,mn}^{(q)} \\ t_{yx,mn}^{(q)} & t_{yy,mn}^{(q)} \end{bmatrix}, \tag{3}$$

where the first and second subscripts denote the polarizations of the transmitted and incident waves, respectively. For the x-polarized feed, $E_x^q = A_{mn}^q e^{-jk_0 R_{mn}^q}$ and $E_y^q = 0$, where $R_{mn}^q = \sqrt{(x_{mn} - x_q)^2 + y_{mn}^2 + z_{mn}^2}$ is the distance from the qth feed to the mnth unit cell. The transmitted field of the mnth unit cell can then be expressed as:

$$\begin{bmatrix} E_{x,mn}^q \\ E_{y,mn}^q \end{bmatrix} = \begin{bmatrix} t_{xx,mn}^{(q)} & t_{xy,mn}^{(q)} \\ t_{yx,mn}^{(q)} & t_{yy,mn}^{(q)} \end{bmatrix} \begin{bmatrix} E_x^q \\ E_y^q \end{bmatrix} \tag{4}$$

For the ideal polarization-conversion state, $t_{xx,mn}^{(q)} \approx 0$, $|t_{yx,mn}^{(q)}| \approx 1$, and $E_y^q = 0$. Therefore, the transmitted field is mainly y-polarized and can be simplified as:

$$E_{y,mn}^q = E_x^q t_{yx,mn}^{(q)} = A_{mn}^q e^{j\left(\angle t_{yx,mn}^{(q)} - k_0 R_{mn}^q\right)}. \tag{5}$$

Therefore, for the expected transmitted beam directed toward $(\theta^{(t)}, \phi^{(t)})$, the phase distribution of the mnth sub-meta-atom 2 unit cell under the excitation of the qth feed in the bidirectional radiation mode is determined by:

$$\varphi_{mn,\mathrm{bi}}^{(q)} = k_0 \Big[\sqrt{(x_{mn} - x_q)^2 + y_{mn}^2 + z_{mn}^2} - x_{mn} \sin\theta^{(t)} \cos\phi^{(t)} - y_{mn} \sin\theta^{(t)} \sin\phi^{(t)} \Big]. \tag{6}$$

In the unidirectional radiation mode, the stacked meta-atom is illuminated simultaneously by the qth feed and its virtual image. First, the response of the mnth meta-atom in the stacked metasurface layers under the illumination of the qth feed can be described using the following Jones matrix:

$$\mathbf{R}_{mn}^{(q)} = \begin{bmatrix} r_{xx,mn}^{(q)} & r_{xy,mn}^{(q)} \\ r_{yx,mn}^{(q)} & r_{yy,mn}^{(q)} \end{bmatrix}, \tag{7}$$

The electric field received by the mnth unit cell from the qth feed and its virtual image can then be expressed as:

$$\begin{bmatrix} E_{x,mn}^q \\ E_{y,mn}^q \end{bmatrix} = \begin{bmatrix} r_{xx,mn}^{(q)} & r_{xy,mn}^{(q)} \\ r_{yx,mn}^{(q)} & r_{yy,mn}^{(q)} \end{bmatrix} \begin{bmatrix} E_x^q + \tilde{E}_x^q \\ E_y^q + \tilde{E}_y^q \end{bmatrix} \tag{8}$$

Here, $\tilde{E}_x^q = A_{mn}^q e^{-jk_0 \tilde{R}_{mn}^q}$ and $\tilde{E}_y^q = A_{mn}^q e^{-jk_0 \tilde{R}_{mn}^q}$ are the electric-field components produced by the virtual image. In addition, $\tilde{R}_{mn}$ denotes the distance from the virtual feed to the mnth stacked unit cell. For the ideal polarization-conversion state, $r_{xx,mn}^{(q)} \approx 0$, $|r_{yx,mn}^{(q)}| \approx 1$, and $E_y^q + \tilde{E}_y^q = 0$. Therefore, the received field is mainly y-polarized and can be simplified as:

$$E_{y,mn}^q = E_x^q t_{yx,mn}^{(q)} = A_{mn}^q e^{j\angle t_{yx,mn}^{(q)}} (e^{-jk_0 R_{mn}^q} + e^{-jk_0 \tilde{R}_{mn}^q}) \tag{9}$$

Here, $\angle t_{yx,mn}^{(q)}$ corresponds to the phase of the mnth unit cell in the stacked metasurface. Finally, the phase distribution of the mnth stacked meta-atom under the excitation of the qth feed can be expressed as:

Authorized licensed use limited to: UNIVERSITY COLLEGE CORK. Downloaded on September 23,2026 at 13:28:03 UTC from IEEE Xplore. Restrictions apply.
© 2026 IEEE. All rights reserved, including rights for text and data mining and training of artificial intelligence and similar technologies. Personal use is permitted, but republication/redistribution requires IEEE permission. See https://www.ieee.org/publications/rights/index.html for more information.

This article has been accepted for publication in IEEE Internet of Things Journal. This is the author's version which has not been fully edited and content may change prior to final publication. Citation information: DOI 10.1109/JIOT.2026.3727129

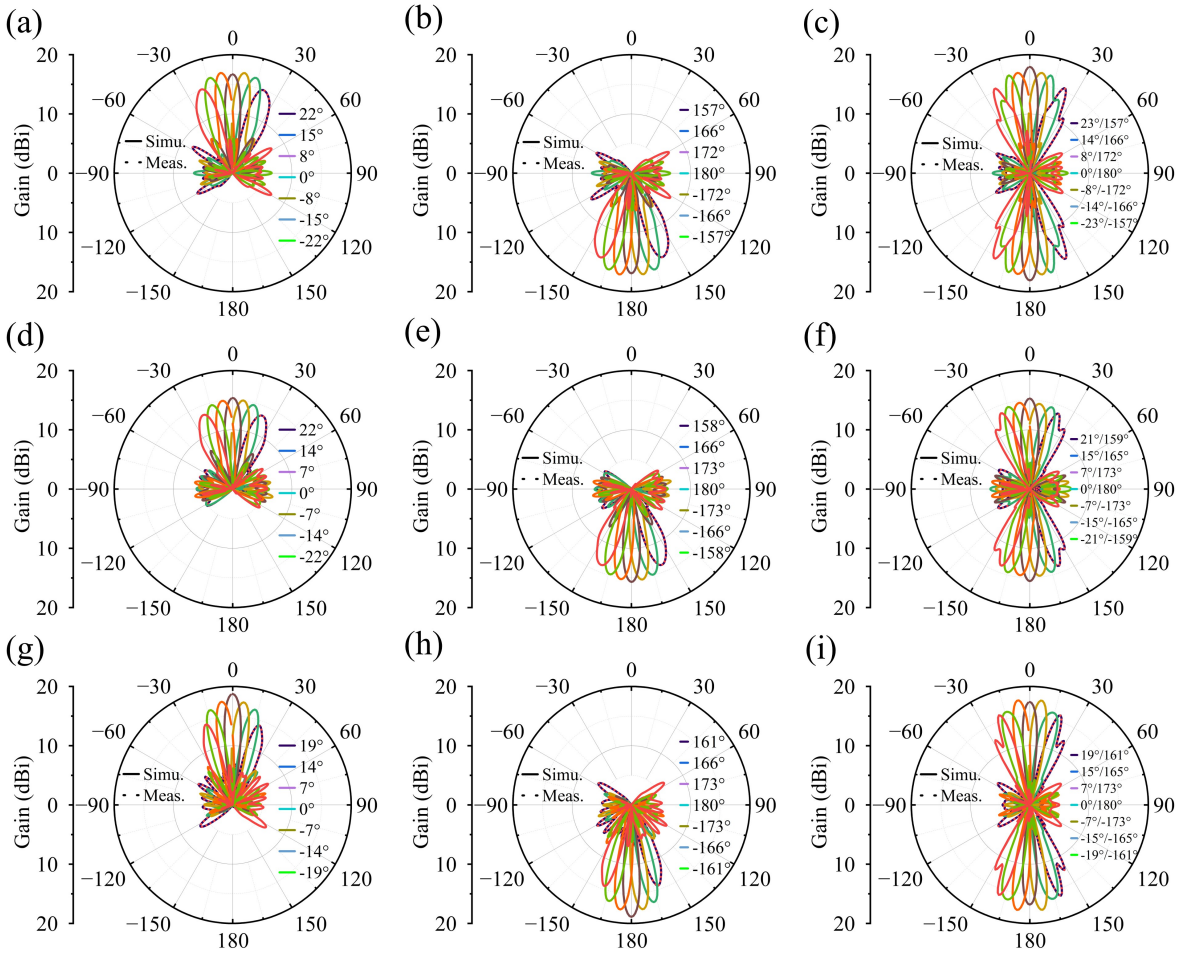


Fig. 9. Radiation patterns of beam-scanning in the xz-plane with small steering angles state. Measured and simulated scanning beams in (a) forward unidirectional radiation at 10 GHz, (b) backward unidirectional radiation at 10 GHz, (c) bidirectional radiation states at 10 GHz, (d) forward unidirectional radiation at 9.5 GHz, (e) backward unidirectional radiation at 9.5 GHz, (f) bidirectional radiation states at 9.5 GHz, (g) forward unidirectional radiation at 10.5 GHz, (h) backward unidirectional radiation at 10.5 GHz, (i) bidirectional radiation states at 10.5 GHz.

$$\phi^{(q)}_{mn,un} = \Big[-\arg(e^{-jk_0R^q_{mn}} + e^{-jk_0\tilde{R}^q_{mn}}) - k_0(x_{mn}\sin\theta^{(t)}\cos\phi^{(t)} - y_{mn}\sin\theta^{(t)}\sin\phi^{(t)}) \Big] \quad (10)$$

Here, $-\arg\left(e^{-jk_0R^q_{mn}} + e^{-jk_0\tilde{R}^q_{mn}}\right)$ represents the phase of $e^{-jk_0R^q_{mn}} + e^{-jk_0\tilde{R}^q_{mn}}$. According to ray-tracing theory, in the unidirectional radiation mode, the distance in the z-direction between the virtual antenna and the metasurface is $3z_{mn}$, that is, $\tilde{R}^q_{mn} = \sqrt{(x_{mn}-x_q)^2 + y^2_{mn} + 9z^2_{mn}}$. In both the bidirectional and unidirectional radiation modes, different feeds require slightly different unit-cell phase distributions. To make a tradeoff among the scanning angles produced by different feeds, the required phase distributions can be averaged using the (2), giving the final unit-cell phase distribution. Moreover, the seven feed ports are arranged along the x-axis symmetrically with respect to the yoz-plane. When the sub-meta-atom 1 layer is rotated clockwise or anticlockwise by 90°, as shown in Fig. 6, the phase distributions in the two rotation states are mirrored about the yoz-plane. Therefore, exciting the corresponding symmetric feed ports produces beams with equal but opposite elevation angles.

To intuitively present the operation principle, the 2D electric E-field distribution and 3D radiation pattern of proposed structures in transmit mode and reflect mode is shown in Fig. 8. It can be observed that the feed antenna can successfully generate bidirectional and unidirectional radiation beams for the transmit mode and reflect mode, respectively.

V. Implementation and Measurements

A. Antenna Configuration

To validate the scanning performance of the proposed array configuration, a TRA was simulated consisting of seven identical feed antennas sandwiched between two identical 24×24-dimensional metasurfaces. The phase distribution of the metasurface is calculated using (**??**) to guarantee the designed TRA is able to switch between both bidirectional and unidirectional radiation states. The distance between upper and lower layer is 171 mm. Seven feed antennas A1-A7 are

Authorized licensed use limited to: UNIVERSITY COLLEGE CORK. Downloaded on September 23,2026 at 13:28:03 UTC from IEEE Xplore. Restrictions apply.
© 2026 IEEE. All rights reserved, including rights for text and data mining and training of artificial intelligence and similar technologies. Personal use is permitted, but republication/redistribution requires IEEE permission. See https://www.ieee.org/publications/rights/index.html for more information.

This article has been accepted for publication in IEEE Internet of Things Journal. This is the author's version which has not been fully edited and content may change prior to final publication. Citation information: DOI 10.1109/JIOT.2026.3727129

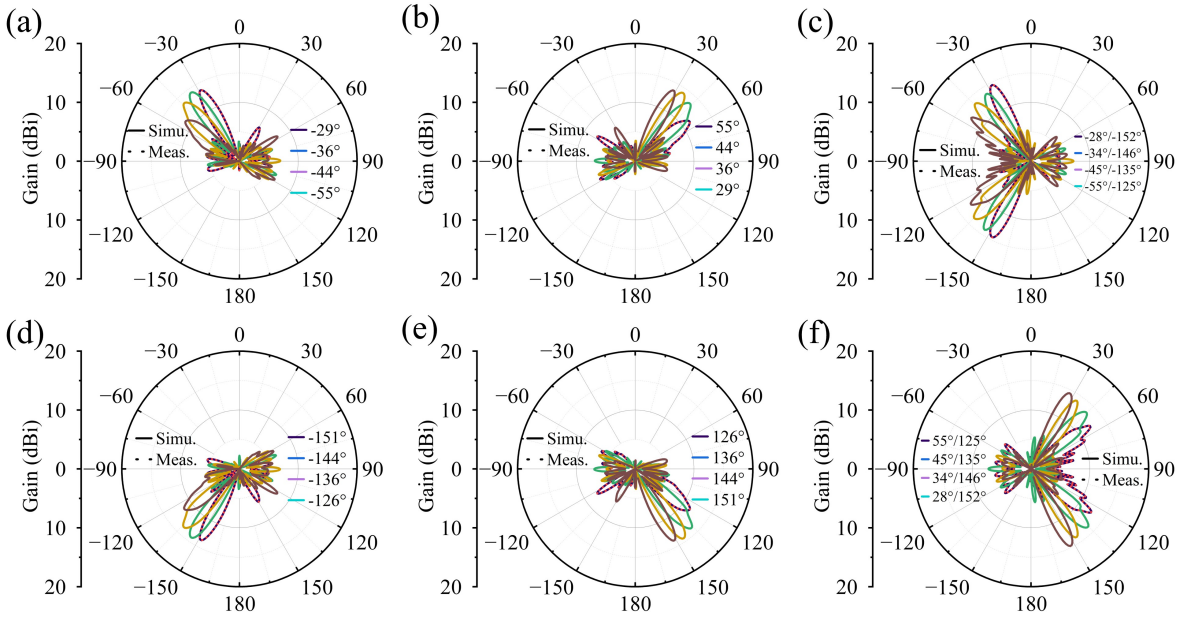


Fig. 10. Radiation patterns of beam-scanning in the xz-plane with large steering angles state at 10 GHz. Measured and simulated scanning beams, in forward direction with rotating sub-metaatom 1 layer (a) clockwise by 90° and (b) anticlockwise by 90°, in backward direction with rotating sub-metaatom 1 layer (c) clockwise by 90° and (d) anticlockwise by 90°, in bidirectional direction with rotating sub-metaatom 1 layer (e) clockwise by 90° and (f) anticlockwise by 90°.

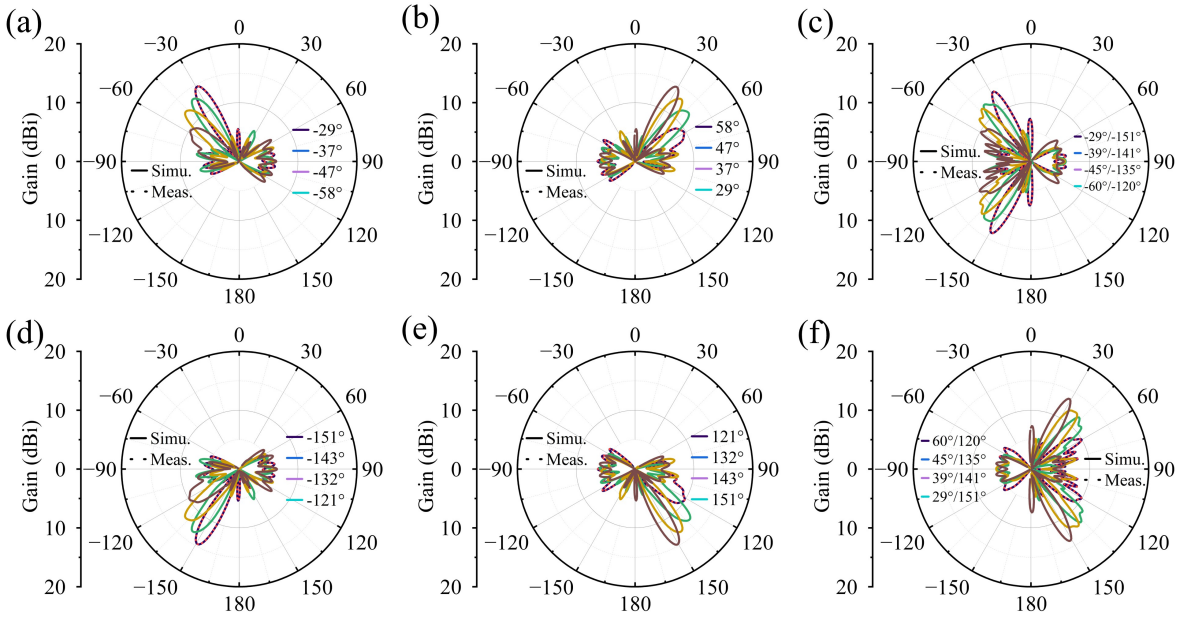


Fig. 11. Radiation patterns of beam-scanning in the xz-plane with large steering angles state at 9.5 GHz. Measured and simulated scanning beams, in forward direction with rotating sub-metaatom 1 layer (a) clockwise by 90° and (b) anticlockwise by 90°, in backward direction with rotating sub-metaatom 1 layer (c) clockwise by 90° and (d) anticlockwise by 90°, in bidirectional direction with rotating sub-metaatom 1 layer (e) clockwise by 90° and (f) anticlockwise by 90°.

equally space arranged along x-axis with coordinates -30, -20, -10, 0, 10, 20, and 30 mm. In the small-angle steering mode, sequential excitation of feeds A1–A7 produces beams at multiple scan angles. For large-angle steering, sequentially exciting A1–A4 or A7–A4 produces beams directed toward the $+x$- or $-x$-axis.

B. Small Steering Angle Operation

As stated above, by configuring the rotation states of both metasurfaces to TM1 or the upper metasurface to TM1 and the lower metasurface to RM1, the proposed TRA can radiate either bidirectional or unidirectional beams within small steering angle ranges. Fig. 9 shows the simulated radiation patterns

Authorized licensed use limited to: UNIVERSITY COLLEGE CORK. Downloaded on September 23,2026 at 13:28:03 UTC from IEEE Xplore. Restrictions apply.
© 2026 IEEE. All rights reserved, including rights for text and data mining and training of artificial intelligence and similar technologies. Personal use is permitted, but republication/redistribution requires IEEE permission. See https://www.ieee.org/publications/rights/index.html for more information.

This article has been accepted for publication in IEEE Internet of Things Journal. This is the author's version which has not been fully edited and content may change prior to final publication. Citation information: DOI 10.1109/JIOT.2026.3727129

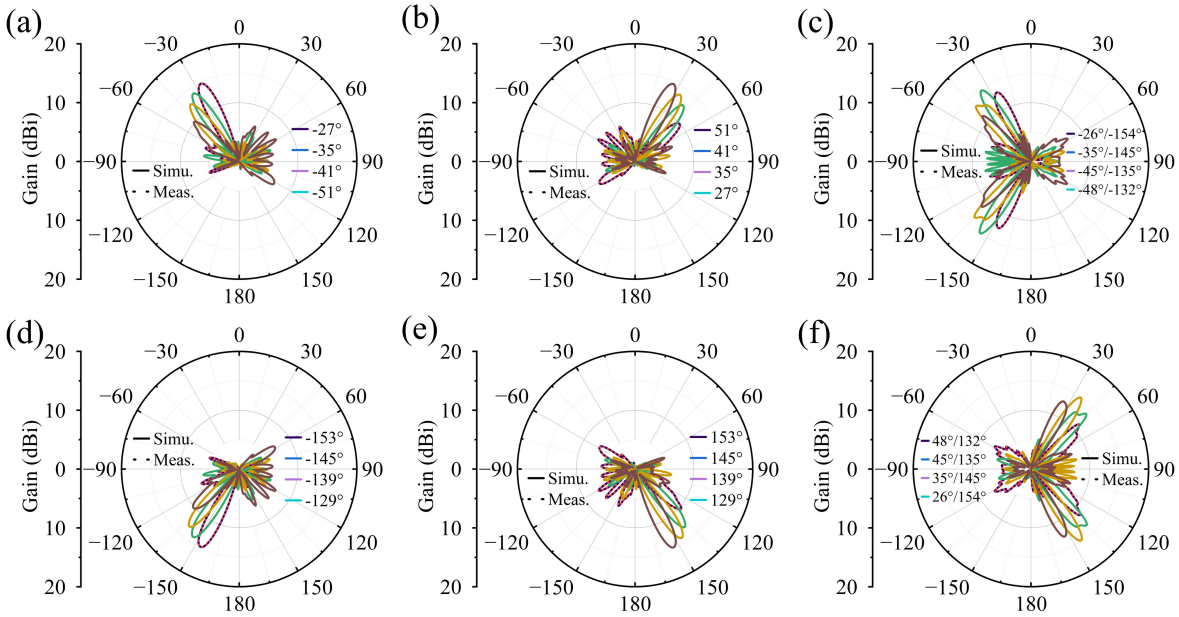


Fig. 12. Radiation patterns of beam-scanning in the xz-plane with large steering angles state at 10.5 GHz. Measured and simulated scanning beams, in forward direction with rotating sub-metaatom 1 layer (a) clockwise by 90° and (b) anticlockwise by 90°, in backward direction with rotating sub-metaatom 1 layer (c) clockwise by 90° and (d) anticlockwise by 90°, in bidirectional direction with rotating sub-metaatom 1 layer (e) clockwise by 90° and (f) anticlockwise by 90°.

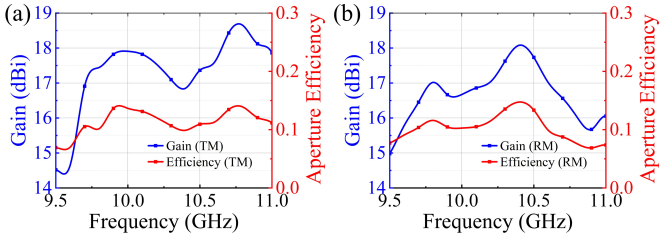


Fig. 13. Simulated peak gain and aperture efficiency versus frequency: (a) TM mode; (b) RM mode.

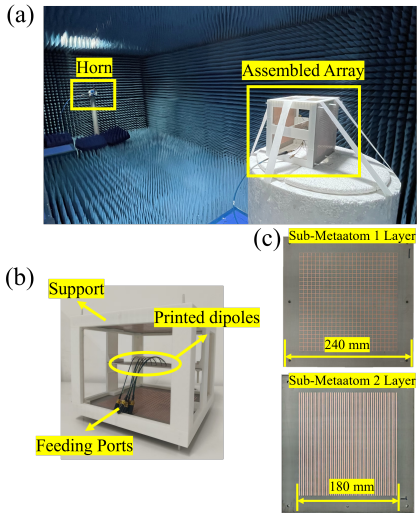


Fig. 14. Experimental characterization of the TRA. (a) Experimental setup. (b) Assembled array. (c) Metasurface layers of sub-metaatom 1 and 2.

of TRA at the frequency points of 9.5, 10, and 10.5 GHz.

For simplicity, the radiation patterns are presented in the xoz-plane, where $0°$ represents the $+z$ direction and $\pm 180°$ represents the $-z$ direction. In the bidirectional radiation mode, the antenna radiates simultaneously toward both the $+z$ and $-z$ directions. In the unidirectional radiation mode, the antenna radiates toward the $+z$ direction when the upper and lower metasurfaces operate in TM1 and RM1, respectively. By interchanging these two states, the radiation direction is switched to the $-z$ direction.

When the feed antennas A1-A7 are excited sequentially, in the unidirectional radiation cases, as shown in Fig. 9a and 9b, the peak gains for the scanning angles of $22°/158°$, $15°/165°$, $8°/172°$, $0°/180°$, $-8°/-172°$, $-15°/-165°$, and $-22°/-158°$ are 14.93, 16.55, 17.02, 16.69, 17.04, 16.52, and 15.08 dBi, respectively. Fig. 9c presents the bidirectional radiation patterns, in which the forward and backward beams are generated simultaneously. Forward and backward beams corresponding to scanning angles of $23°/157°$, $14°/166°$, $8°/172°$, $0°/180°$, $-8°/-172°$, $-14°/-166°$, and $-23°/-157°$ are generated simultaneously at 10 GHz. The corresponding peak gains for these scanning angles are 15.4, 16.8, 17.1, 17.9, 17.1, 16.8, and 15.4 dBi, respectively. Fig. 9d to 9f and Fig. 9g to 9i depict the radiation patterns of TRA at 9.5 GHz and 10.5 GHz, respectively. In the unidirectional radiation states, the radiation patterns at all three frequency points exhibit good steering performance while maintaining low sidelobe levels (SLLs). It can also be observed that the maximum steering angle of the TRA ranging from 10 GHz to 10.5 GHz slightly decreases from 22° to 19° in the forward direction, which is primarily attributed to the effect of beam squint and unit cell dispersion.

Authorized licensed use limited to: UNIVERSITY COLLEGE CORK. Downloaded on September 23,2026 at 13:28:03 UTC from IEEE Xplore. Restrictions apply.
© 2026 IEEE. All rights reserved, including rights for text and data mining and training of artificial intelligence and similar technologies. Personal use is permitted, but republication/redistribution requires IEEE permission. See https://www.ieee.org/publications/rights/index.html for more information.

This article has been accepted for publication in IEEE Internet of Things Journal. This is the author's version which has not been fully edited and content may change prior to final publication. Citation information: DOI 10.1109/JIOT.2026.3727129

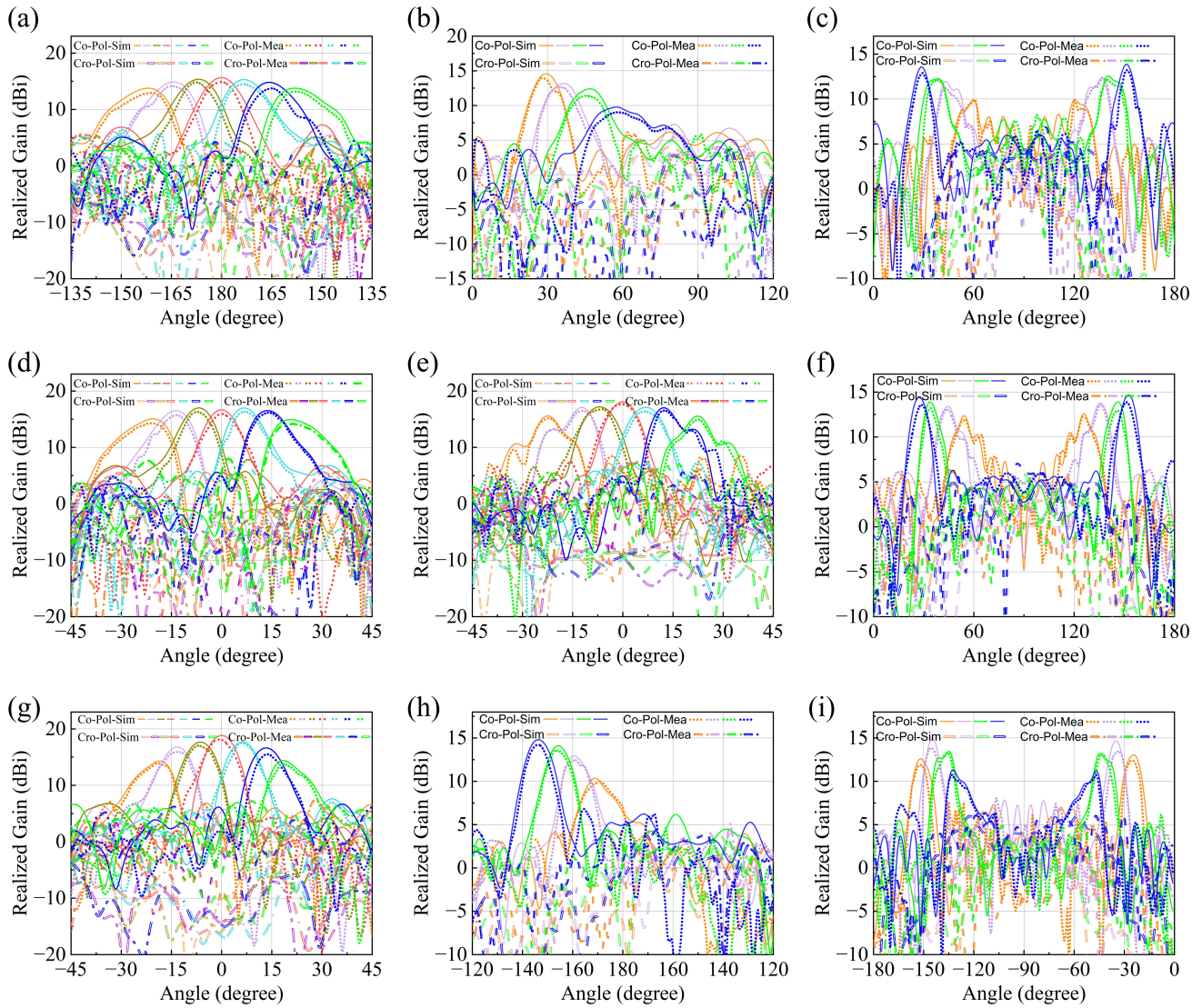


Fig. 15. Comparison between simulated and measured radiation patterns in the xoz-plane. (a)–(c) Backward unidirectional radiation, forward unidirectional radiation, and bidirectional radiation with sub-metaatom layer 1 rotated clockwise by 90°, respectively, at 9.5 GHz. (d)–(f) Forward unidirectional radiation, bidirectional radiation along the $+z$-axis, and bidirectional radiation with sub-metaatom layer 1 rotated clockwise by 90°, respectively, at 10 GHz. (g)–(i) Bidirectional radiation along the $+z$-axis, backward radiation with sub-metaatom layer 1 rotated anticlockwise by 90°, and bidirectional radiation with sub-metaatom layer 1 rotated clockwise by 90°, respectively, at 10.5 GHz.

C. Large Steering Angle Operation

Fig. 10 shows the simulated beam steering patterns of the designed array operating at large steering angles at a frequency of 10 GHz. When the upper sub-meta-atom 1 layer is rotated anticlockwise or clockwise by 90° while the lower metasurface is maintained in RM1, the feed antennas A4-A7/A4-A1 are sequentially excited to generate forward radiation beams with scanning angles of $-29°/29°$, $-36°/36°$, $-44°/44°$, and $-55°/55°$. As shown in Fig. 10a and Fig. 10b, the corresponding peak gains for scanning angles of $-29°/29°$, $-36°/36°$, $-44°/44°$, and $-55°/55°$ are 13.60, 14.21, 13.49, and 11.39 dBi, respectively. Similarly, the radiation patterns steered in the backward directions are presented in Fig. 10d and Fig. 10e. In addition, the bidirectional beam steering patterns obtained when both sub-meta-atom-1 layers are rotated simultaneously anticlockwise or clockwise by 90° are shown in Fig. 10c and Fig. 10f. As observed from Fig. 10f, the feed antennas A1-A4 can be sequentially excited to generate main beams with scanning angles of 55°, 45°, 34°, and 28° in the forward direction, and 125°, 135°, 146°, and 152° in the backward direction. The corresponding peak gains are 12.45, 13.62, 13.98, and 14.43 dBi in the forward direction, and 12.52, 13.78, 13.70, and 14.70 dBi in the backward direction, respectively.

Similarly, Fig.11 and Fig.12 present beam-scanning patterns with large steering angles at 9.5 and 10.5 GHz, respectively. In contrast to unidirectional radiation states, bidirectional patterns generate larger SLLs. The maximum steering angles are 55° and 58° for frequency points of 9.5, and 10.5 GHz, respectively.

Fig. 13 illustrates the gain and aperture efficiency for the TM and RM in the frequency range from 9.5 to 11 GHz.

Authorized licensed use limited to: UNIVERSITY COLLEGE CORK. Downloaded on September 23,2026 at 13:28:03 UTC from IEEE Xplore. Restrictions apply.
© 2026 IEEE. All rights reserved, including rights for text and data mining and training of artificial intelligence and similar technologies. Personal use is permitted, but republication/redistribution requires IEEE permission. See https://www.ieee.org/publications/rights/index.html for more information.

This article has been accepted for publication in IEEE Internet of Things Journal. This is the author's version which has not been fully edited and content may change prior to final publication. Citation information: DOI 10.1109/JIOT.2026.3727129

TABLE I
COMPARISON OF MEASURED RADIATION PERFORMANCE

Ref.	Radiation Type	Frequency (GHz)	Gain Bandwidth	Aperture Efficiency (%)	Dimension (Lowest operating frequency)	Beam-control Method	Beam-scanning Mode	Maximum Scanning Angle	Fabrication Difficulty
[29]	+z, -z	11	22.6% (1 dB)	45.6/48.2	$6.05\lambda_0 \times 6.05\lambda_0 \times 0.471\lambda_0$	N.A.	N.A.	N.A.	Simple
[30]	+z, -z, $\pm$z	10	15% (1 dB)	92/90	$13.02\lambda_0 \times 13.02\lambda_0 \times 0.0067\lambda_0$	N.A.	N.A.	N.A.	Simple
[31]	+z	26	13.1% (1 dB)	N.A.	$9.97\lambda_0 \times 9.97\lambda_0 \times 0.022\lambda_0$	Mechanical control	Unidirectional	$\pm 60^\circ$	Simple
[32]	+z, -z	33	18.7% (1 dB)	N.A.	$10.07\lambda_0 \times 10.07\lambda_0 \times 5.03\lambda_0$	Mechanical control	Unidirectional	$\pm 10^\circ$	Simple
[34]	+z, -z, $\pm$z	9.5	19.9% (3 dB)	19.2/17.3/7.1	$7.04\lambda_0 \times 7.04\lambda_0 \times 0.120\lambda_0$	PIN diodes	Unidirectional/ Bidirectional	$\pm 45^\circ$	Complex
[36]	$\pm$z	5.8	8.4% (1 dB)	8.9/8.1	$6.08\lambda_0 \times 6.08\lambda_0 \times 0.097\lambda_0$	PIN diodes	Bidirectional	$\pm 60^\circ$	Complex
[41]	+z, -z, $\pm$z	9.75	15.4% (3 dB)	13.3/11.9	$11.52\lambda_0 \times 11.52\lambda_0 \times 7.04\lambda_0$	Switched feeds	Unidirectional/ Bidirectional	$\pm 30^\circ$, $\pm 22^\circ$	Moderate
This work	+z, -z, $\pm$z	10	6.1% (1 dB)	13.9/11.6	$5.82\lambda_0 \times 5.82\lambda_0 \times 6.47\lambda_0$	Mechanical control	Unidirectional/ Bidirectional	$\pm 55^\circ$	Simple

As shown in Fig. 13a, the 1-dB bandwidth is approximately 6.1% (9.7–10.3 GHz), and the maximum realized gain at 10.0 GHz is 17.90 dBi for the TM when radiating along normal unidirectional. Meanwhile, as depicted in Fig. 13b, the 1-dB bandwidth is approximately 5.0% (9.6–10.1 GHz), and the maximum realized gain at 9.8 GHz is 17.02 dBi for the RM when radiating along normal bidirectional. In addition, the maximum aperture efficiency for bidirectional and unidirectional radiating state are 13.9% and 11.6%, respectively. Although the designed ABBA structure, which introduces strong capacitive coupling between layers, enables high transmission amplitude at the resonant frequency, it also results in a narrow phase shift bandwidth due to significant electromagnetic (EM) characteristic variations away from the resonant frequencies [45].

D. Measurement and Discussion

To demonstrate the correctness of proposed configuration, a prototype with overall dimensions of $264 \times 264 \times 216\ mm^3$ was fabricated and measured, as depicted in Fig. 14. The radiation patterns of assembled array were measured in an anechoic chamber using a standard X-Band horn antenna, as shown in Fig. 14a. Fig. 14b presents the overall configuration of proposed antenna. Specifically, 3-D printing technology was used to print the mechanical support bracket for realizing the assembly of the printed dipole antennas and stacked metasurface aperture. Antenna consists of five PCB layers, and each PCB layer can be manually rotated to guarantee the variation of operation mode. Fig. 14c and d shows the sub-metaatom 1 and sub-metaatom 2 layers, where the PCB dimension is $240 \times 240\ mm^2$ and the metasurface aperture dimension is $180 \times 180\ mm^2$.

Several examples of the simulated and measured co- and cross-polarized radiation patterns in the xoz-plane at 9.5, 10.0, and 10.5 GHz are shown in Fig. 15. As illustrated in Fig. 15(a), (d), and (g), the measured and simulated co-polarized patterns agree well in the main-beam regions at small steering angles. For instance, in Fig. 15(d), the measured peak gains in the forward unidirectional mode at scanning angles of -23°, -14°, -8°, 0°, 8°, 14°, and 23° are 14.21, 15.89, 16.37, 16.01, 16.38, 16.41, and 14.19 dBi, respectively. These values are no more than 0.8 dB lower than their simulated counterparts.

For the bidirectional mode with large steering angles, as shown in Fig. 15(i), an increase in the measured SLLs is observed at 10.5 GHz. This is mainly caused by the mismatch between the desired phase distribution and the actual phase compensation provided by the metasurface. Nevertheless, the simulated and measured beam directions agree well, and the measured scanning-gain reduction remains within approximately 1 dB.

The cross-polarized components are generally much lower than the co-polarized main beams. For most of the presented beams, the measured cross-polarization level in the co-polarized main-beam direction is more than 10 dB below the co-polarized peak, with a median difference of approximately 17 dB. The remaining differences between the simulated and measured patterns are mainly attributed to fabrication and assembly tolerances and measurement uncertainties.

A performance comparison between the proposed transmit-reflect-array and previous designs is presented in Table I. The main contribution of this work is a mechanically controlled TRA that supports switchable $+z$, $-z$, and simultaneous $\pm z$ radiation, together with wide-angle beam scanning up to $\pm 55^\circ$. It also has a compact lateral size of $5.82\lambda_0 \times 5.82\lambda_0$. Although its overall height is relatively large, some reported profiles include only the metasurface thickness and exclude the feed antenna and feed-to-aperture distance, whereas this work reports the complete antenna size.

In the present prototype, the operating modes were manually

Authorized licensed use limited to: UNIVERSITY COLLEGE CORK. Downloaded on September 23,2026 at 13:28:03 UTC from IEEE Xplore. Restrictions apply.
© 2026 IEEE. All rights reserved, including rights for text and data mining and training of artificial intelligence and similar technologies. Personal use is permitted, but republication/redistribution requires IEEE permission. See https://www.ieee.org/publications/rights/index.html for more information.

This article has been accepted for publication in IEEE Internet of Things Journal. This is the author's version which has not been fully edited and content may change prior to final publication. Citation information: DOI 10.1109/JIOT.2026.3727129

switched by rotating the corresponding PCB layers by 90°. For practical implementation, the rotatable layers can be mounted in rigid frames with bearings and driven by motors. The feasibility and reliability of similar mechanical mechanisms have been demonstrated by other researchers [46], [47] After considering aperture inertia, acceleration, and positioning, the practical switching time is expected to be several hundred milliseconds.

Compared with PIN-diode-based solutions, mechanical control is slower and requires additional supporting structures [48]. Motor lifetime, wear, backlash, and positioning errors may also affect long-term operation. However, the passive aperture reduces RF loss, fabrication complexity, and control-power consumption. Therefore, this approach is mainly intended for fixed IoT applications where the coverage mode changes slowly and deployment cost is an important concern.

VI. Conclusion

In this article, a novel bidirectional multilayer beam steering TRA based on mechanical control technique is introduced. By rotating the angle of different metasurface layers, three different radiation states along +z, -z, or $\pm$z direction can be realized. The measured results are consistent with the numerical simulated results, which demonstrate the bidirectional functionalities of proposed multilayer TRA.

Due to its switchable capability between bidirectional and unidirectional radiation, this technology holds significant potential toward real-world IoT applications, including but not limited to radar systems, UAV relay communications, indoor wireless communications, and cellular mobile communications. It is worth emphasizing that several challenges remain and require further investigation, such as the design of wideband and high-efficiency unit cells to improve gain bandwidth, achieve higher aperture efficiency, enable wide-angle beam scanning, and mitigate feed blockage.

References

[1] M. Ahmed, A. Wahid, S. S. Laique, W. U. Khan, A. Ihsan, F. Xu, S. Chatzinotas, and Z. Han, "A survey on STAR-RIS: Use cases, recent advances, and future research challenges," *IEEE Internet Things J.*, vol. 10, no. 16, pp. 14689–14711, Aug. 2023.

[2] M. Katwe, K. Singh, B. Clerckx, and C.-P. Li, "Improved spectral efficiency in STAR-RIS aided uplink communication using rate splitting multiple access," *IEEE Trans. Wireless Commun.*, vol. 22, no. 8, pp. 5365–5382, Aug. 2023.

[3] W. Yu, C. Mao, J. Ou, and X. Y. Zhang, "Shared-aperture dual-circularly polarized phased array antenna with small frequency ratio for satellite-assisted IoT communications," *IEEE Internet Things J.*, vol. 13, no. 3, pp. 4537–4545, 2026.

[4] C. Ding, X. Gao, X. Bu, and J. An, "Large-frequency-ratio dual-band shared-aperture conformal transmit-reflect-array antenna with independent beam control for UAV-based space-air-ground emergency communication networks," *IEEE Trans. Antennas Propag.*, 2026.

[5] J. Z. Moghaddam, H. M. Firouzjaei, and M. Ardebilipour, "UAV-enabled IoT networks: A SWIPT energy harvesting architecture with relay support for disaster response," *IEEE Internet Things J.*, 2025.

[6] P. Mei, G. F. Pedersen, and S. Zhang, "Development of wideband transmitarray antennas with adaptive bidirectional beam reconfigurability for mm-wave IoT applications," *IEEE Internet Things J.*, vol. 12, no. 16, pp. 34044–34053, 2025.

[7] Z. Liu, X. Chu, D. López-Pérez, and N. Tang, "Deployment strategy of intelligent omni-surface-assisted outdoor-to-indoor millimeter-wave communications," *IEEE Trans. Wireless Commun.*, vol. 23, no. 12, pp. 19172–19182, 2024.

[8] R. Z. Jiang, C. K. Shen, H. D. Li, Q. Y. Zhou, Z. H. Fu, Z. X. Wang, T. T. Ye, J. Y. Dai, L. K. Yang, J. Ma, and others, "A metasurface-enabled green-smart window for intelligent wireless communications with high visible transparency and low infrared emissivity," *Nature Commun.*, 2026.

[9] X. Bai, L. Wang, F. Zhang, J. Chen, W. Chen, H.-X. Xu, and R. Jin, "Wideband radiation-type programmable metasurface-enabled high-precision beam modulating for IoT applications," *IEEE Internet Things J.*, vol. 12, no. 14, pp. 28823–28834, 2025.

[10] L. Wang, H. Shi, X. Chen, B. Qu, J. Yi, A. Zhang, Z. Xu, and H. Liu, "Multibeam metasurface antenna enabled by orbital angular momentum demultiplexing feeding for IoT communication," *IEEE Internet Things J.*, vol. 10, no. 18, pp. 16169–16182, 2023, doi: 10.1109/JIOT.2023.3267424.

[11] Y.-X. Sun and K. W. Leung, "Millimeter-wave substrate-based dielectric reflectarray," *IEEE Antennas Wireless Propag. Lett.*, vol. 17, no. 12, pp. 2329–2333, 2018.

[12] G. Yang, G. Jiang, Y. Zhang, Y. Ma, L. Wang, Z. Xing, D. Psychogiou, and L. Wang, "Dual-polarized antenna with flexible pattern steering based on digital meta-surface for satellite-assisted mobile communication," *IEEE Internet Things J.*, vol. 13, no. 7, pp. 14141–14150, 2026, doi: 10.1109/JIOT.2025.3648644.

[13] W. Lee, M. Yi, J. So, and Y. J. Yoon, "Non-resonant conductor reflectarray element for linear reflection phase," *Electron. Lett.*, vol. 51, no. 9, pp. 669–671, 2015.

[14] T. Hong, X.-P. Shi, and X.-S. Liang, "Synthesis of sparse linear array for directional modulation via convex optimization," *IEEE Trans. Antennas Propag.*, vol. 66, no. 8, pp. 3959–3972, Aug. 2018.

[15] L. Tosi, A. Benoni, *et al.*, "Mask-constrained synthesis of domino-like tiled phased arrays," *Prog. Electromagn. Res. B*, vol. 95, pp. 173–195, 2022.

[16] Y. Ma, Y. Guo, Q. Luo, Y. Zhou, G. Yang, and S. Gao, "Phase-only pattern synthesis of domino tiling irregular arrays based on deep reinforcement learning and gradient-descent optimization," *IEEE Trans. Antennas Propag.*, early access, 2025, doi: 10.1109/TAP.2025.3567185.

[17] M. Iqbal, T. Ashraf, M. Zubair, S. M. Jameel, M. Jazib, and J.-Y. Pan, "A comprehensive survey on reconfigurable intelligent surfaces (RIS) and STAR-RIS for next-generation wireless networks," *Discover Appl. Sci.*, vol. 7, no. 11, p. 1253, 2025.

[18] H. Ju, D. Kim, H. V. Poor, and D. Hong, "Bi-directional beamforming and its capacity scaling in pairwise two-way communications," *IEEE Trans. Wireless Commun.*, vol. 11, no. 1, pp. 346–357, 2011.

[19] Z.-H. Fu, X.-S. Yang, and B.-Z. Wang, "Low-cost conformal transmit-reflect-array antenna for unmanned aerial vehicle relay communications," *IEEE Trans. Antennas Propag.*, 2024.

[20] Y. Chen, X. Yang, and J. Gao, "3D Janus plasmonic helical nanoapertures for polarization-encrypted data storage," *Light Sci. Appl.*, vol. 8, no. 1, p. 45, 2019.

[21] X. Zhang, H. Zhang, L. Sun, X. Wang, K. Long, and V. C. M. Leung, "STAR-RIS-aided UAV communication for next generation multiple access with resource allocation," *IEEE J. Sel. Topics Signal Process.*, 2024.

[22] S. Cao, Z. Zhang, X. Fu, and J. Wang, "Pattern-reconfigurable bidirectional antenna design using the characteristic mode analysis," *IEEE Antennas Wireless Propag. Lett.*, vol. 20, no. 1, pp. 53–57, 2020.

[23] M. Liu, Z. J. Zhai, F. Lin, and H. J. Sun, "Wideband quad-polarization-reconfigurable bidirectional antenna with a simple wideband switchable feeding network," *IEEE Antennas Wireless Propag. Lett.*, vol. 22, no. 6, pp. 1346–1350, 2023.

[24] A. Alhamed, G. Gültepe, and G. M. Rebeiz, "64-element 16–52-GHz transmit and receive phased arrays for multiband 5G-NR FR2 operation," *IEEE Trans. Microw. Theory Techn.*, vol. 71, no. 1, pp. 360–372, 2022.

[25] X. Zhong, H.-X. Xu, L. Chen, W. Li, H. Wang, and X. Shi, "An FSS-backed broadband phase-shifting surface array with multimode operation," *IEEE Trans. Antennas Propag.*, vol. 67, no. 9, pp. 5974–5981, 2019.

[26] W. Li, Y. Wang, S. Sun, and X. Shi, "An FSS-backed reflection/transmission reconfigurable array antenna," *IEEE Access*, vol. 8, pp. 23904–23911, 2020.

[27] M. N. Jazi, M. R. Chaharmir, J. Shaker, and A. R. Sebak, "Broadband transmitarray antenna design using polarization-insensitive frequency selective surfaces," *IEEE Trans. Antennas Propag.*, vol. 64, no. 1, pp. 99–108, Jan. 2015.

[28] W. Song, Q. Xue, Y. Cai, N. Guo, K. Liu, S. Li, and H. Ding, "A single-layer reflect-transmit-array antenna with polarization-dependent operation," *IEEE Access*, vol. 9, pp. 167928–167935, 2021.

Authorized licensed use limited to: UNIVERSITY COLLEGE CORK. Downloaded on September 23,2026 at 13:28:03 UTC from IEEE Xplore. Restrictions apply.
© 2026 IEEE. All rights reserved, including rights for text and data mining and training of artificial intelligence and similar technologies. Personal use is permitted, but republication/redistribution requires IEEE permission. See https://www.ieee.org/publications/rights/index.html for more information.

This article has been accepted for publication in IEEE Internet of Things Journal. This is the author's version which has not been fully edited and content may change prior to final publication. Citation information: DOI 10.1109/JIOT.2026.3727129

[29] S. Liu and Q. Chen, "A wideband, multifunctional reflect-transmit-array antenna with polarization-dependent operation," *IEEE Trans. Antennas Propag.*, vol. 69, no. 3, pp. 1383–1392, 2020.

[30] F. Yang, R. Deng, S. Xu, and M. Li, "Design and experiment of a near-zero-thickness high-gain transmit-reflect-array antenna using anisotropic metasurface," *IEEE Trans. Antennas Propag.*, vol. 66, no. 6, pp. 2853–2861, Jun. 2018.

[31] M. I. Abbasi, M. H. Dahri, M. H. Jamaluddin, N. Seman, M. R. Kamarudin, and N. H. Sulaiman, "Millimeter wave beam steering reflectarray antenna based on mechanical rotation of array," *IEEE Access*, vol. 7, pp. 145685–145691, 2019.

[32] Z. Zhai, F. Lin, Y. Yang, and H. Sun, "Additively manufactured wideband low-profile bidirectional 2-D beam-scanning antenna using double folded transmitarrays with curved polarizers," *IEEE Trans. Antennas Propag.*, vol. 72, no. 1, pp. 476–486, Jan. 2023.

[33] M. Wang, S. Xu, F. Yang, and M. Li, "A 1-bit bidirectional reconfigurable transmit-reflect-array using a single-layer slot element with PIN diodes," *IEEE Trans. Antennas Propag.*, vol. 67, no. 9, pp. 6205–6210, 2019.

[34] H. Yu, P. Li, J. Su, Z. Li, S. Xu, and F. Yang, "Reconfigurable bidirectional beam-steering aperture with transmitarray, reflectarray, and transmit-reflect-array modes switching," *IEEE Trans. Antennas Propag.*, vol. 71, no. 1, pp. 581–595, 2022.

[35] Y. Zhao, D. Wang, H. Gu, P. Chen, Y. Liang, M. Du, W. Liu, and L. Ge, "Design of a novel wideband reconfigurable transmit-reflect-array antenna utilizing twin lines," *IEEE Trans. Antennas Propag.*, vol. 72, no. 3, pp. 2897–2902, 2024.

[36] M. Xiang, Y. Xiao, J. Deng, S. Xu, and F. Yang, "Simultaneous transmitting and reflecting reconfigurable array (STAR-RA) with independent beams," *IEEE Trans. Antennas Propag.*, vol. 71, no. 10, pp. 8338–8343, Oct. 2023.

[37] Z.-Y. Yu, Y.-H. Zhang, S.-Y. He, H.-T. Gao, H.-T. Chen, and G.-Q. Zhu, "A wide-angle coverage and low scan loss beam steering circularly polarized folded reflectarray antenna for millimeter-wave applications," *IEEE Trans. Antennas Propag.*, vol. 70, no. 4, pp. 2656–2667, 2021.

[38] Y. Hu, W. Hong, and Z. H. Jiang, "A multibeam folded reflectarray antenna with wide coverage and integrated primary sources for millimeter-wave massive MIMO applications," *IEEE Trans. Antennas Propag.*, vol. 66, no. 12, pp. 6875–6882, Dec. 2018.

[39] F. Arpin, J. Shaker, and D. A. McNamara, "Multi-feed single-beam power-combining reflectarray antenna," *Electron. Lett.*, vol. 40, no. 17, pp. 1035–1037, Aug. 2004.

[40] A. Gómez-Álvarez, Á. F. Vaquero, M. Arrebola, and M. R. Pino, "Multibeam compact reflectarray antenna with low scan loss and wide-angle performance using a multi-feed configuration," *IEEE Open J. Antennas Propag.*, 2024.

[41] F. Qin, Y. Liu, C. Gu, L. Zeng, W. Cheng, H. Zhang, and S. Gao, "Multibeam hybrid transmitarray based on polarization rotating metasurface with reconfigurable bidirectional radiation," *IEEE Trans. Antennas Propag.*, 2024.

[42] T. Cai, G.-M. Wang, J.-G. Liang, Y.-Q. Zhuang, and T.-J. Li, "High-performance transmissive meta-surface for C-/X-band lens antenna application," *IEEE Trans. Antennas Propag.*, vol. 65, no. 7, pp. 3598–3606, Jul. 2017.

[43] W. Ji, T. Cai, X. Zheng, and P. Urbach, "Highly efficient and broadband achromatic transmission metasurface to refract and focus in microwave region," *Laser Photon. Rev.*, vol. 16, no. 1, p. 2100333, Jan. 2022.

[44] S. A. Matos, E. B. Lima, J. R. Costa, C. A. Fernandes, and N. J. Fonseca, "Design of a 40 dBi planar bifocal lens for mechanical beam steering at Ka-band," in *Proc. 10th Eur. Conf. Antennas Propag. (EuCAP)*, Apr. 2016, pp. 1–4.

[45] N. Gagnon, A. Petosa, and D. A. McNamara, "Research and development on phase-shifting surfaces (PSSs)," *IEEE Antennas and Propagation Magazine*, vol. 55, no. 2, pp. 29–48, 2013.

[46] G. Mackertich-Sengerdy, L. Kang, S. D. Campbell, and D. H. Werner, "Reconfigurable metamirrors based on compliant mechanisms," *Adv. Funct. Mater.*, vol. 36, no. 10, p. e16276, 2026.

[47] Q. Xu, X. Su, X. Zhang, L. Dong, L. Liu, Y. Shi, Q. Wang, M. Kang, A. Alù, S. Zhang, and others, "Mechanically reprogrammable Pancharatnam–Berry metasurface for microwaves," *Adv. Photon.*, vol. 4, no. 1, pp. 016002–016002, 2022.

[48] M. Mirmozafari, Z. Zhang, M. Gao, J. Zhao, M. M. Honari, J. H. Booske, and N. Behdad, "Mechanically reconfigurable, beam-scanning reflectarray and transmitarray antennas: A review," *Appl. Sci.*, vol. 11, no. 15, p. 6890, 2021.

Authorized licensed use limited to: UNIVERSITY COLLEGE CORK. Downloaded on September 23,2026 at 13:28:03 UTC from IEEE Xplore. Restrictions apply.
© 2026 IEEE. All rights reserved, including rights for text and data mining and training of artificial intelligence and similar technologies. Personal use is permitted, but republication/redistribution requires IEEE permission. See https://www.ieee.org/publications/rights/index.html for more information.